catalysts

MDPI

Article

Magnetically Assembled Electrode Incorporating Self-Powered Tourmaline Composite Particles: Exploiting Waste Energy in Electrochemical Wastewater Treatment

Bo Zhang [1], Dan Shao [1,*], Yaru Wang [1], Hao Xu [2] and Haojie Song [1]

[1] School of Materials Science and Engineering, Shaanxi University of Science & Technology, Xi'an 710021, China; zhang081251@163.com (B.Z.); wangyaru@sust.edu.cn (Y.W.); songhaojie@sust.edu.cn (H.S.)
[2] Department of Environmental Engineering, Xi'an Jiaotong University, Xi'an 710049, China; xuhao@mail.xjtu.edu.cn
* Correspondence: shaodan@sust.edu.cn

Abstract: A magnetically assembled electrode (MAE) is a modular electrode format in electrochemical oxidation wastewater treatment. MAE utilizes magnetic forces to attract the magnetic catalytic auxiliary electrodes (AEs) on the main electrode (ME), which has the advantages of high efficiency and flexible adjustability. However, the issue of the insufficient polarization of the AEs leaves the potential of this electrode underutilized. In this study, natural tourmaline (Tml) particles with pyroelectric and piezoelectric properties were utilized to solve the above issue by harvesting and converting the waste energy (i.e., the joule heating energy and the bubble striking mechanical energy) from the electrolysis environment into additional electrical energy applied on the AEs. Different contents of Tml particles were composited with Fe_3O_4/Sb-SnO_2 particles as novel AEs, and the structure–activity relationship of the novel MAE was investigated by various electrochemical measurements and orthogonal tests of dye wastewater treatment. The results showed that Tml could effectively enhance all electrochemical properties of the electrode. The optimal dye removal rate was obtained by loading the AEs with 0.2 g·cm^{-2} when the Tml content was 4.5 wt%. The interaction of current density and Tml content had a significant effect on the COD removal rate, and the mineralization capacity of the electrode was significantly enhanced. The findings of this study have unveiled the potential application of minerals and energy conversion materials in the realm of electrochemical oxidation wastewater treatment.

Keywords: electrochemical oxidation; magnetically assembled electrode; tourmaline; ultrasound; dye wastewater

check for updates

Academic Editor: Annalisa Vacca

Received: 25 November 2024
Revised: 9 December 2024
Accepted: 17 December 2024
Published: 24 December 2024

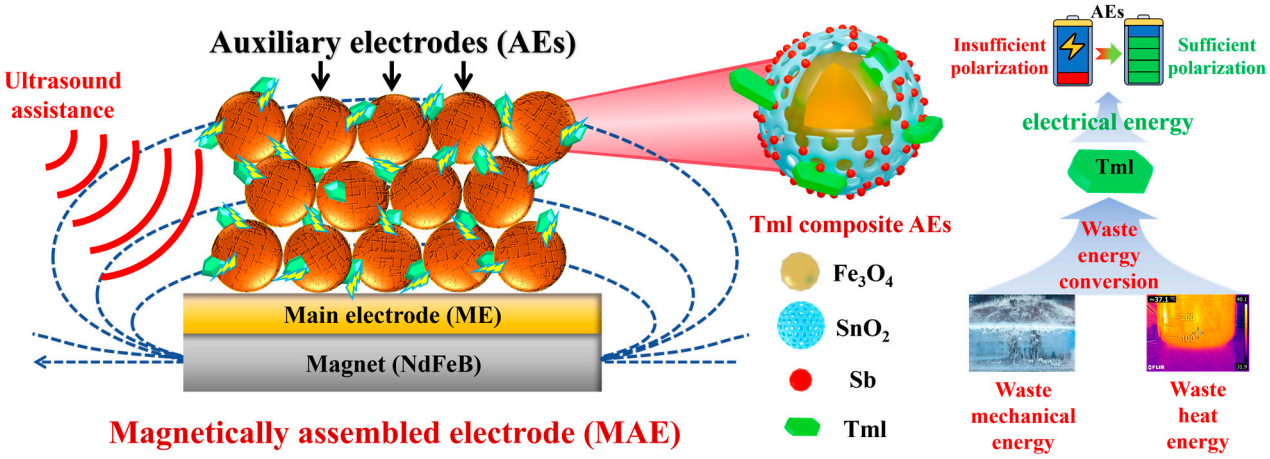
Citation: Zhang, B.; Shao, D.; Wang, Y.; Xu, H.; Song, H. Magnetically Assembled Electrode Incorporating Self-Powered Tourmaline Composite Particles: Exploiting Waste Energy in Electrochemical Wastewater Treatment. *Catalysts* **2025**, *15*, 2. https://doi.org/10.3390/catal15010002

Copyright: © 2024 by the authors. Licensee MDPI, Basel, Switzerland. This article is an open access article distributed under the terms and conditions of the Creative Commons Attribution (CC BY) license (https://creativecommons.org/licenses/by/4.0/).

1. Introduction

Electrochemical oxidation (EO) is a green and efficient wastewater treatment technology [1–5]. The efficiency and cost of this technology are largely determined by the anode structure and composition [4]. In contrast to conventional 2D planar electrode and 3D electrode structures, a magnetically assembled electrode (MAE) is an innovative modular electrode configuration comprising a permanent magnet (NdFeB), a 2D planar main electrode (ME), and auxiliary electrodes (AEs) particles with high catalytic activity. This novel design is also referred to as a "2.5D electrode" (Scheme 1) [6]. MAE attracts AEs to the ME surface through a flexible magnetic force, thereby increasing the number of active sites. Meanwhile, the electrode composition and structure can be adjusted in situ according to the requirements of wastewater treatment by changing the AEs type and loading amount, thus

ensuring that wastewater treatment is efficient at all times. However, many interfaces exist in this modular electrode (physically bonded electrocatalysts), and the AEs are indirectly polarized via the ME. These inherent features result in a loss of driving force for electrode polarization at the interfaces between the ME and AEs, as well as at the interfaces of the AEs, which in turn, gives rise to the inherent issue of insufficient and uneven polarization of the AEs. As a consequence, the full potential of the additional active sites is not realized, and the performance of the MAE is limited.



Scheme 1. Structure of the magnetically assembled electrode (MAE) and the novel tourmaline composite auxiliary electrodes (AEs) particles in this study and the schematic diagram of the waste energy conversion of tourmaline in electrolysis.

In recent years, our research group has been dedicated to addressing the aforementioned bottleneck issue by establishing efficient charge transfer pathways at the ME–AEs interface as well as within the layers of the AEs. On the one hand, the charge transfer barrier at the ME–AEs interface could be successfully reduced by adopting ME materials with low oxygen evolution potential (such as RuO_2-IrO_2 and IrO_2-Ta_2O_5) [7–9] or highly conductive ME materials (such as graphite and Pt) [8,10]. On the other hand, increasing the contact area among AEs (e.g., carbonaceous AEs materials) also resulted in notable progress [10–12]. However, the issue has not been effectively resolved as the polarization of AEs still relies on the external circuit and ME. Therefore, if AEs are equipped with energy harvesting and conversion capabilities to directly harness energy from wastewater, this aforementioned bottleneck issue could be truly overcome. For instance, certain novel materials exhibiting piezoelectric and pyroelectric properties (e.g., $BaTiO_3$ and $BiFeO_3$) are capable of converting mechanical or heat energy into electrical energy. Researchers have integrated these energy-converting materials with photocatalysts to enhance the efficiency of photocatalytic water treatment [13–15]. Therefore, integrating materials with piezoelectric or pyroelectric properties into the AEs could theoretically yield comparable effects. Tourmaline (Tml) exhibits remarkable piezoelectric and pyroelectric properties, and as a natural inorganic mineral, it is characterized by the absence of secondary pollution and is readily available at a low cost [16,17]. By integrating Tml with AEs, the pyroelectric and piezoelectric properties of Tml are harnessed to convert Joule heat energy and mechanical energy from bubble impacts during the electrolysis process into additional electrical energy [18,19], which is then supplied in situ to the AEs, thereby theoretically addressing the above issue. Furthermore, ultrasound has the capability to induce a Joule heating effect and mechanical vibrational effect [20], and could therefore be utilized to enhance the prominence of Tml's function (see Scheme 1).

In light of the aforementioned considerations, this study has synthesized a novel composite AEs by integrating Tml with typical AEs materials Fe_3O_4/Sb-SnO_2. As a result, an upgraded MAE with exceptional catalytic activity and remarkable energy harvesting and conversion properties has been achieved. Among various ME (e.g., Ti/RuO_2-IrO_2, graphite, or Pt), Ti/Sb-SnO_2 with a limited polarization capability [7] was selected and magnetically coupled to the aforementioned composite AEs to construct MAE (see Scheme 1). To assess the potential differences in energy conversion efficiency of the composite AEs across various energy conditions, the degradation of azo fluorescent dye wastewater (acid red G, ARG) was conducted under three current densities (5 mA·cm^{-2}, 20 mA·cm^{-2}, and 50 mA·cm^{-2}) and three ultrasound powers (0 W, 60 W, and 120 W), and the electrochemical oxidation degradation mechanisms of organic contaminants under these different energy conditions were investigated. Meanwhile, since ultrasound could also activate peroxymonosulfate (PDS) to generate sulfate radicals (SO_4^{-}) [21,22], the impact of PDS was investigated. Orthogonal tests were designed based on the above multiple factors and levels to explore the significance factors and optimal levels affecting the organic contaminants' removal rate and COD removal rate. This study aims to provide a more efficient anode electrocatalyst selection for EO water treatment and to provide a preliminary theoretical basis and technical support for its future application. The findings of this study also have unveiled the potential application of minerals and energy conversion materials in the realm of EO wastewater treatment.

2. Results and Discussion

2.1. Material Characterization Results

The results of morphological and structural characterization of the novel Tml composite AEs and their related particles are shown in Figure 1. SEM images show that natural Tml exhibits a prismatic conical structure (Figure 1a), and the particle size is mainly distributed around 10 μm; however, there are also particle agglomerates present with 30~40 μm particles. EDS elemental analysis reveals that the main components of Tml are O, Si, Al, Fe, Ca, and Na (Figure S3a). The SEM image of the AEs particles Fe_3O_4/Sb-SnO_2 is shown in Figure 1b, and their particle sizes mainly range between 5 and 10 μm. The element distribution clearly shows that the Sb-SnO_2 catalytic layer on the AEs provides good coverage of magnetic particles (Figure 1c). The SEM images of the two AEs prepared by mixing different proportions of Tml are shown in Figure 1d,e, where it can be seen that the particles become rough and the particle size distribution is around 10 μm. The ferroelectric property of Tml used in this study is shown in Figure 1f. The obvious residual polarization (~0.6 mC·m^{-2}) verifies Tml's ferroelectricity (multiple test result on the ferroelectric properties of Tml are shown in Figure S8), which is also meets the necessary condition for its pyroelectricity and piezoelectricity [23].

The XRD results for the three AEs are presented in Figure 1g. With an increasing content of Tml, the characteristic peaks of Tml become increasingly pronounced, and the SnO_2 characteristic peaks sharpen significantly. This observation indicates that the incorporation of Tml effectively enhances the grain size of SnO_2 and facilitates a strong interaction between the SnO_2 catalyst layer and Tml [24]. The structural diagrams of MAE composed of novel composite AEs with different Tml contents and the schematic diagrams of the conducting channels are shown in Figure 1h. When the Tml content is 4.5 wt%, only a portion of the AEs incorporate Tml, that is, the relatively intact conductive channels between them. In contrast, when the Tml content is 16 wt%, the majority of the AEs are successfully composited with Tml and there are AEs containing multiple Tml particles. However, since Tml is an insulating material, the conductive channels between the AEs may be affected.

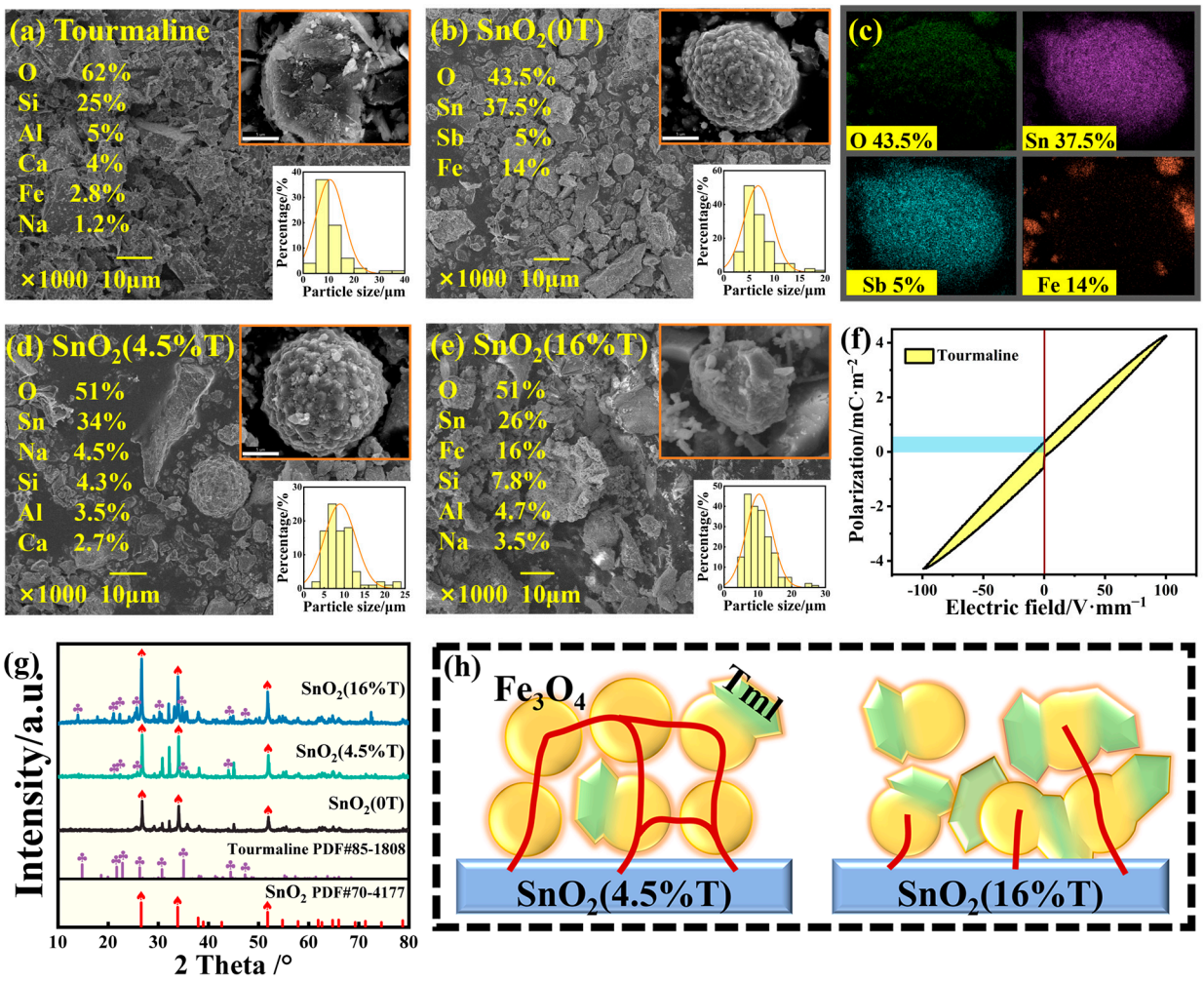


Figure 1. Preparation processes of different AEs particles in this study and their material characterization results: (**a**) SEM image and particle size distribution of Tml. (**b**) SEM images and particle size distribution of SnO_2(0T). (**c**) EDS elemental content distribution of SnO_2(0T). SEM images and particle size distribution of (**d**) SnO_2(4.5%T) and (**e**) SnO_2(16%T). (**f**) Tml polarization curves; (**g**) XRD images of the three AEs. (**h**) Schematic diagram of the distribution of different ratios of tourmaline doping.

2.2. Electrochemical Characterization Results

To explore the enhancement effects of novel Tml composite AEs on the electrocatalytic performance of MAE, the 2D Ti/Sb-SnO_2 and three Tml composite AEs (SnO_2(0T), SnO_2(4.5%T), SnO_2(16%T)) are assembled as MAE, and the impact of different AEs loading amounts (0 g·cm^{-2}, 0.2 g·cm^{-2}, and 0.5 g·cm^{-2}) are investigated. As shown in Figure 2a–f, the above seven electrodes are tested for electrochemical characterization (different ranges of CV and EIS). The 2D Ti/Sb-SnO_2 has a lower C_{dl} (35.37 mF·cm^{-2}) and q_T (0.087 C) due to the smaller electrochemically active surface area [25] and limited number of active sites. In addition, the lower $I_{2.5V}$ and higher OEP also indicate the poor OER activity of this electrode. The introduction of 0.2 g·cm^{-2} SnO_2(0%T) has not resulted in any significant changes to the electrochemical performance of the electrode. While the AEs contribute to an increase in geometric area, issues related to the insufficient polarization of the AEs persisted, preventing the effective activation of its active sites. Consequently, neither the total number of active sites on the electrode nor the effective electrochemical active surface area experienced a meaningful increase. The introduction of SnO_2(4.5%T) resulted in a 22.02% increase in the C_{dl} and a 40.92% increase in the q_T of the MAE. This observation suggests that the active sites on the AEs are effectively activated by a small content of

Tml, leading to an enhancement in additional effective electrochemical active surface area. Additionally, the R_{ct} of the MAE decreased while the $I_{2.5V}$ increased, with minimal change observed in the OEP. This suggests that the enhancement in the MAE's OER activity is primarily attributed to an increase in effective electrochemical active surface area rather than a modification of the material's intrinsic activity. When the MAE consists of SnO_2(16%T), all electrochemical performance metrics of the MAE, with the exception of OEP, exhibit a significant decline. This is mainly because Tml itself is not conductive, and excessive Tml has a negative impact on the charge transfer on the AEs (consistent with the situation expressed in Figure 1h).

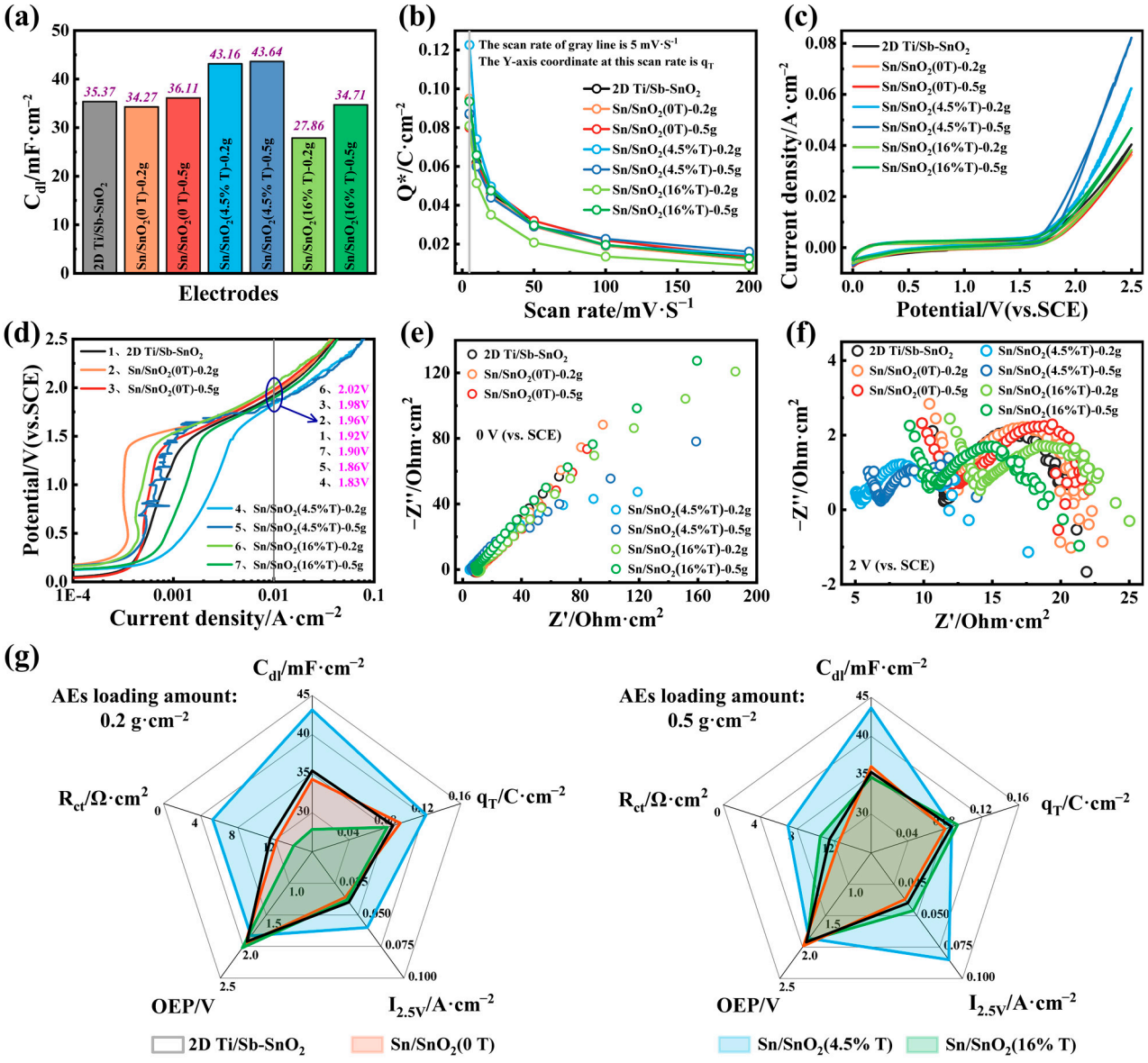


Figure 2. Electrochemical characterization of 2D Ti/Sb-SnO_2 and each group of MAE: (**a**) Double-layer capacitance value (C_{dl}). (**b**) Voltametric charge (Q*) obtained at different potential scan rates and the corresponding q_T. (**c**) CV curves (potential range: 0~2.5 V (vs. SCE), scan rate: 0.01 V·s^{-1}). (**d**) Tafel plots of LSV curves. (**e**,**f**) Nyquist plots (equilibrium potential: 0 V and 2 V (vs. SCE), frequency range: 0.1~10^5 Hz). (**g**) Comprehensive comparison radar plots of key electrochemical performance metrics.

As the AEs loading amount increases to 0.5 g·cm^{-2}, the thickness of the AEs' layer increases, leading to more pronounced issues related to insufficient and uneven polarization.

Consequently, when the MAE consists of SnO_2(0%T), its electrochemical performance closely resembles that of 2D Ti/Sb-SnO_2. Upon the introduction of 0.5 g·cm^{-2} SnO_2(4.5%T), the enhancement in electrochemical performance, with the exception of OEP and q_T, was comparable to that observed with 0.2 g·cm^{-2} SnO_2(4.5%T), thereby confirming the significance of Tml. However, despite a substantial increase in C_{dl}, the q_T for MAE exhibited minimal variation due to the excessive thickness of the AEs layer, which hindered contact between active sites at the ME–AEs interface and the electrolyte. Upon the introduction of 0.5 g·cm^{-2} SnO_2(16%T), the beneficial effects attributed to Tml nearly vanished, while the aforementioned negative impacts associated with excessive Tml continued to persist.

Additionally, the key electrochemical performance metrics (C_{dl}, q_T, $I_{2.5V}$, OEP (vs. SCE), and R_{ct}) for the seven groups of MAE were extracted from Figure 2a–f and represented in a radar plot for comprehensive comparison (Figure 2g). The area of the radar plot distinctly indicates that the overall enhancement in electrochemical performance of the 0.2 g·cm^{-2} SnO_2(4.5%T) is superior to that of all other MAEs.

2.3. ARG Degradation Results

The individual and synergistic effects of ultrasound and PDS in electrochemical oxidation are investigated by one-factor degradation experiments. Figure 3 shows the degradation of Acid Red G (ARG) (250 mL, 200 mg·L^{-1}) after treatment for 90 min under various ultrasonic and PDS conditions. As shown in Figure 3a, the introduction of PDS and ultrasound in the electrochemical oxidation system improved the degradation rate of ARG by the four electrodes, and the enhancement effect of ultrasound is significant. For 2D Ti/Sb-SnO_2, the effect of PDS on the ARG removal rate is not significant in the pre-reaction period and plays a positive role in the late reaction period. This is because ultrasound accelerates the ARG removal rate by generating HO· through cavitation. Furthermore, the vibration of ultrasound contributes to the improvement of contaminants' mass transfer at the solution/electrode interface. The ARG removal rate is further increased when ultrasound is used in conjunction with PDS, as ultrasound activates PDS at an early stage. The rapid collapse of cavitation bubbles generates local hot spots characterized by elevated temperature and pressure in their vicinity, facilitating heat transfer that enables PDS to produce SO_4^{-}· [26].

The catalytic ability of MAE is further enhanced when 2D Ti/Sb-SnO_2 is assembled with AEs. This is because the MAE structure has a larger specific surface area. In addition, the significant enhancement of the ARG removal rate by MAE in the presence of ultrasound is attributed to the fact that ultrasound vibration exposes more effective active sites on the electrode. Among the three MAEs, Sn/SnO_2(4.5%T)-0.2 g shows the best degradation ability of ARG. This is because Tml converts the heat energy generated by the Joule heating effect of the electric current and the mechanical energy generated by the impact of bubbles during water decomposition into electrical energy that can be used by the catalyst particles (compared with Sn/SnO_2(0T)-0.2 g). In addition, the large amount of Tml cuts off the electron transfer between MEs and AEs, leading to a decrease in the ARG removal rate by Sn/SnO_2(16%T)-0.2 g.

Figure 3b shows the change in chemical oxygen demand (COD) of the ARG solution after 90 min of degradation under different conditions of ultrasound and PDS. It can be clearly seen that the COD of the ARG solution decreased more after the introduction of ultrasound and PDS (consistent with the ARG removal rate). When Tml is introduced in the AEs, the COD of the ARG solution decreases further. The COD of the ARG solution degraded by Sn/SnO_2(4.5%T)-0.2 g finally decreased to 15 mg·L^{-1}, which proves the enhanced mineralization ability of AEs after the introduction of composite Tml. The COD of the ARG solution degraded by Sn/SnO_2(4.5%T)-0.2 g eventually decreased to 8 mg·L^{-1}.

This result again demonstrates the enhanced catalytic ability of AEs after the introduction of composite Tml.

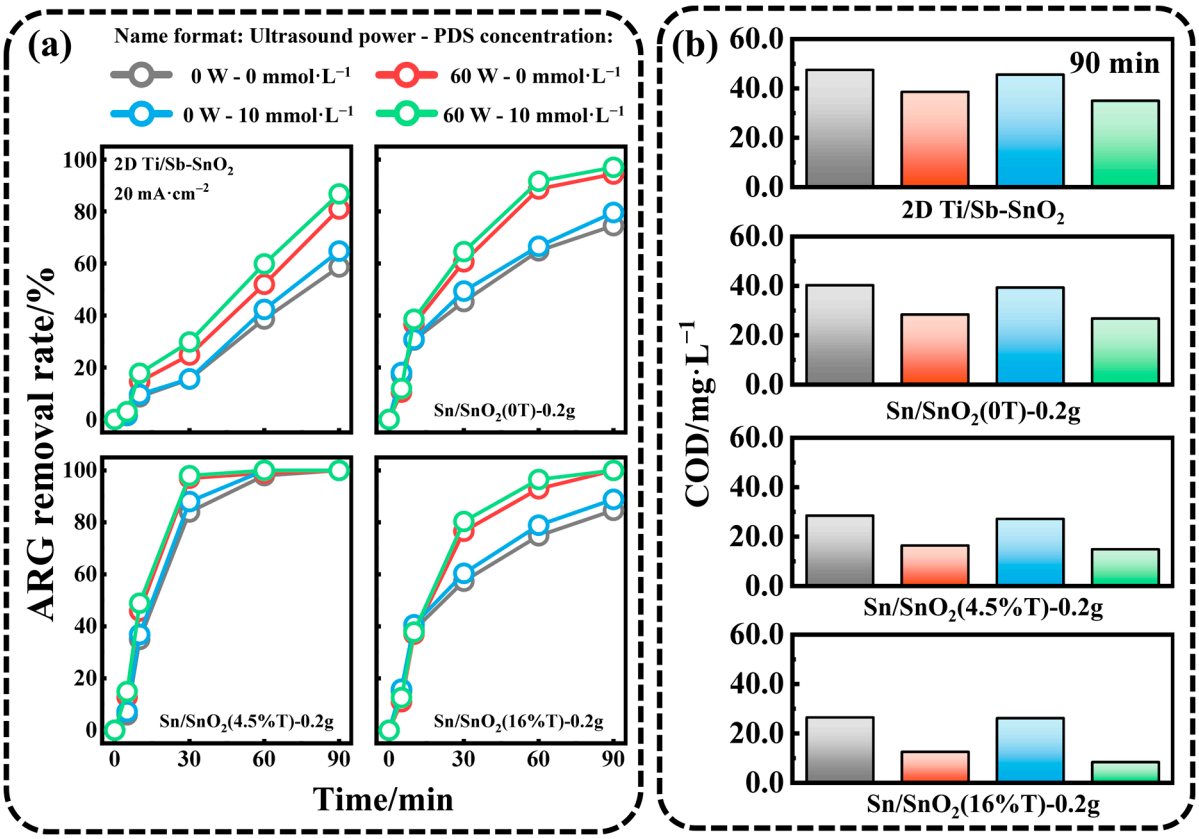


Figure 3. One-factor experiments on the degradation of ARG (250 mL, 200 mg·L^{-1}) by four electrodes composed of Ti/Sb-SnO_2 for 90 min under four experimental conditions: (**a**) ARG removal rate versus time; (**b**) COD of ARG solution after 90 min of degradation.

2.4. Orthogonal Tests Results

Orthogonal tests were conducted using the $L_{27}(3^{13})$ orthogonal table (Tables S1 and S2) with six main single factors and three interaction factors (Table S1). The statistical results of the orthogonal tests with the ARG removal rate of 30 min as the indicator are shown in Figure 4. The contribution rate of the significant single factors and interaction factors to the ARG removal rate after 30 min of degradation are shown in Figure 4a. In descending order of contribution rate, they are AEs loading amount (C, 67.9%), current density × AEs type (B × D, 11.1%), current density (B, 8.62%), ultrasound power (F, 3.43%), PDS concentration (E, 3.23%), AEs type × AEs loading amount (D × C, 2.67%), AEs type × ultrasound power (D × F, 1.06%) and error (2.04%). The results indicate that the AEs loading amount exerts the most pronounced influence, highlighting the advantages of MAE. Furthermore, significant interactions are observed between AEs type and other factors. Because the current density and ultrasound power significantly affects the magnitude of additional energy, the significance of the interaction between the above factors and the different contents of Tml in the AEs can be attributed to the effective utilization of waste heat energy and mechanical energy by Tml. However, since the contribution rate analysis cannot reflect the degree of influence of each factor level, a further assessment of the main effects of each single factor and the general average factor is needed [27,28].

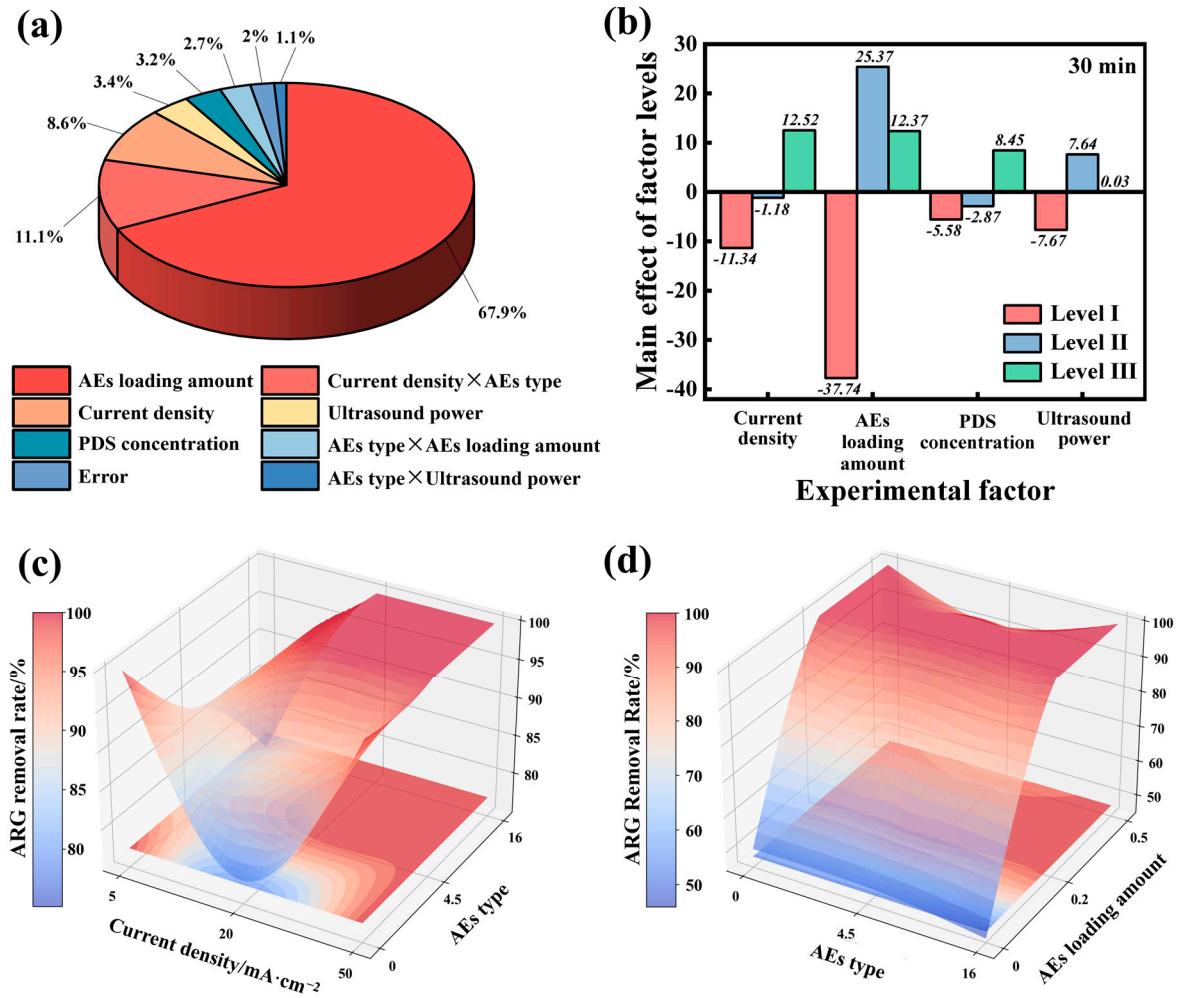


Figure 4. Results of orthogonal test analysis based on ARG removal rate after 30 min of degradation: (**a**) Distribution of contributions of significant single and interaction factors to experimental results. (**b**) Significant single factor main effects at each level. (**c**,**d**) Space curved surface plot of the effect of different interaction factors on ARG removal rate.

The main level effect of the significant single factor is shown in Figure 4b, which shows that Level II (0.2 g·cm^{-2}) of the AEs loading amount has a significant positive effect on the ARG removal rate, whereas an excessive AEs loading amount rather diminishes this advantage, which is in full agreement with the above results of electrochemical characterization, and also matches with the results of previous studies by our research group on the MAE [8–11]. Level III of current density (50 mA·cm^{-2}) also has a more pronounced positive effect, with greater current density not only generating more radicals and bringing about more charge transfer, but likewise providing more waste energy to be utilized by Tml. In addition, there are also the small positive effects of Level III of PDS concentration (20 mmol·L^{-1}) and Level II of the ultrasound power (60 W) on the ARG removal rate.

The space curved surface plots of the effect of the interaction of current density × AEs type on the ARG removal rate are shown in Figure 4c. Among the three composite AEs particles with different Tml contents, SnO_2(4.5%T) exhibits a more satisfactory ARG removal rate at all three current densities, indicating that a moderate amount of Tml content does not only affect the catalytic activity of the AEs, but also efficiently utilizes the additional waste energy. In contrast, the advantage of SnO_2(16%T) is only demonstrated at high current densities, since the additional waste energy is limited and the conductivity is poor at low current densities (consistent with electrochemical characterization). Figure 4d shows

the space curved surface plot of the effect on the ARG removal rate under the interaction of AEs type × AEs loading amount, showing the ARG removal rate was significantly affected by the AEs loading amount (consistent with the contribution rate of the ARG removal rate) and that 0.2 g·cm^{-2} SnO_2(4.5%T) was able to obtain the optimal degradation effect.

The statistical results of the orthogonal tests with the COD removal rate of 90 min as the indicator are shown in Figure 5. The contribution rate of the significant single factors and interaction factors to the ARG removal rate after 30 min of degradation are shown in Figure 5a. In descending order of contribution rate, they are current density × AEs type (B × D, 33.48%), error (14.19%), AEs loading amount (C, 12.1%), ultrasound power (F, 10.78%), AEs type × AEs loading amount (D × C, 10.73%), AEs type (D, 9.54%), and current density (B, 9.17%). The contribution rate of current density or AEs type to the COD removal rate was not significant, but the contribution rate was greatly enhanced after the interaction of current density × AEs type. This indicates that AEs can only be significantly activated when waste energy and Tml are co-present, demonstrating that the energy conversion effect of Tml is the key to COD removal.

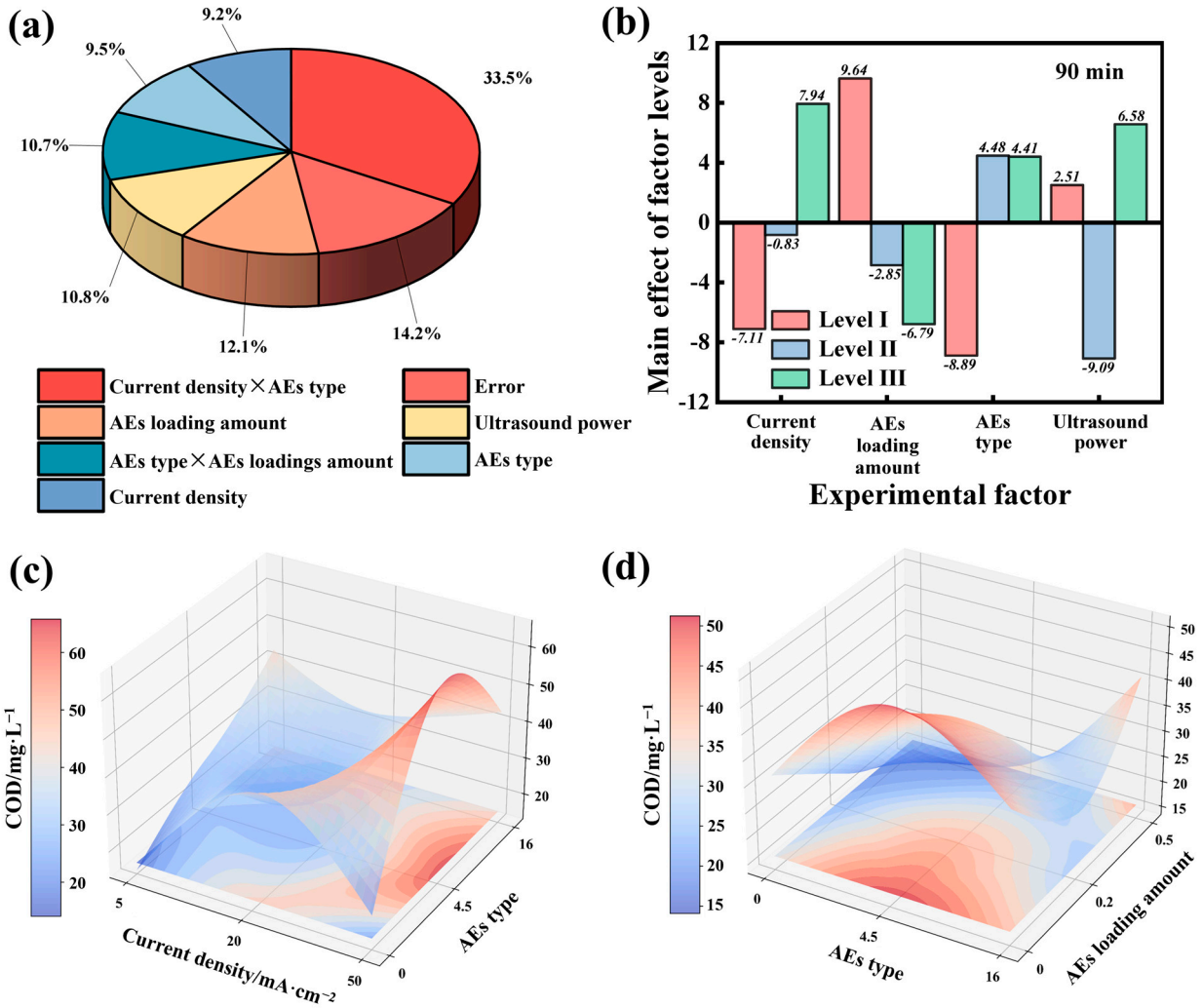


Figure 5. Results of orthogonal test analysis based on COD removal rate after 90 min of degradation: (**a**) Distribution of contributions of significant single and interaction factors to experiment results. (**b**) Significant single factor main effects at each level. (**c**,**d**) Space curved surface plot of the effect of different interaction factors on COD removal rate.

The main level effects of significant single factors affecting the COD removal rate are shown in Figure 5b. Level III of current density (50 mA·cm^{-2}) had the most significant pos-

itive effect on COD removal rate. Level II and Level III of AEs loading amount performed poorly. Combined with Figure 5b, this was mainly due to the accelerated degradation of ARG after the loading of the AEs, leading to the generation of a large number of small-molecule products (which are more readily detected by COD digestion compared to ARG). In addition, there was a positive effect for Level II and Level III of AEs type, demonstrating that Tml can effectively enhance the mineralization of contaminants by MAE.

The space curved surface plots of the effect of the interaction of current density × AEs type on the COD removal rate are shown in Figure 5c. The COD removal rate of a MAE loaded with SnO_2(4.5%T) or SnO_2(16%T) can be increased by 22.82~192.57% across three current densities, suggesting that the presence of Tml mitigates the issues of insufficient and uneven polarization in the AEs, activates its active sites (consistent with the electrochemical characterization), and consequently enhances the overall mineralization capacity of the MAE. Figure 5d shows the space curved surface plots of the effect on the COD removal rate under the interaction of AEs type × AEs loading amount. After the introduction of Tml into AEs, the COD removal rate was improved from 14.11~20.48% to 37.80~41.14%. This further proves the effectiveness of Tml in solving the bottleneck problem of MAE.

3. Experiments

3.1. MAE Preparation

Ti/Sb-SnO_2 ME was successfully synthesized on a 4 cm × 3 cm titanium plate (Baotai, Jinzhou, China) using an electrodeposition-thermal decomposition method [7]. In preparing the composite AEs, a certain amount of Fe_3O_4 particles was first mixed with butyl titanate in the ratio of 1:2, and the Fe_3O_4/TiO_x particles containing the TiO_x layer were obtained after drying and roasting. The above particles were then calcined with tin dioxide, antimony trioxide, binder, and 2000-mesh purchased Tml (Shijiazhuang Tourmaline Minerals, Shijiazhuang, China) by high-temperature solid-phase synthesis to obtain composite AEs with different Tml contents (Figure 1a), which were designated as SnO_2(0T) (without Tml), SnO_2(4.5%T) (4.5% Tml content), and SnO_2(16%T) (16% Tml content).

The ME and AEs were assembled using NdFeB magnets. The AEs loading amounts were set to 0 g·cm^{-2}, 0.2 g·cm^{-2}, and 0.5 g·cm^{-2}, respectively. The electrode without AEs was named 2D Ti/Sb-SnO_2. The remaining six MAEs were named Sn/SnO_2(0T)-0.2 g, Sn/SnO_2(0T)-0.5 g, Sn/SnO_2(4.5T)-0.2 g, Sn/SnO_2(4.5%T)-0.5 g, Sn/SnO_2(16%T)-0.2 g, and Sn/SnO_2(16%T)-0.5 g, respectively.

3.2. Material Characterization

The morphology of the Ti/Sb-SnO_2 was examined using a scanning electron microscope (SEM: SU8100, Hitachi, Tokyo, Japan). The morphologies and surface element contents of Tml and AEs were characterized by a scanning electron microscopy with an energy disperse spectroscopy (SEM/EDS: Aztec X-MaxN 80, Oxford Instruments, Oxford, UK). The ferroelectric properties of Tml were tested using a polyK ferroelectric test station. The structural and compositional analyses of Tml and AEs were carried out by an X-ray diffractometer (XRD: D/max-2200PC, Rigaku, Tokyo, Japan).

3.3. Electrochemical Characterization

All measurements were performed in a three-electrode cell containing a 0.5 M Na_2SO_4 solution by using a potentiostat/galvanostat (CS310H, CorrTest, Wuhan, China). The MAE acted as the working electrode (effective area 1 cm^2), the copper slice was used as the counter electrode (electrode spacing 1 cm), and the saturated calomel electrode (SCE: 0.241 V vs. NHE) was used as the reference electrode. Low potential range cyclic voltammograms (CV) were obtained between 0 and 0.3 V (vs. SCE) at scan rates of 0.005 V·s^{-1}, 0.01 V·s^{-1},

0.02 $V \cdot s^{-1}$, 0.05 $V \cdot s^{-1}$, 0.1 $V \cdot s^{-1}$, and 0.2 $V \cdot s^{-1}$, respectively. A series of obtained response current densities were subjected to linear fitting against the corresponding scanning rates to determine the electrical double-layer capacitor (C_{dl}) of the electrode, which reflects its effective electrochemical active surface area [10]. In addition, the voltametric charge (Q*) of the electrode (reflecting the number of active sites) was obtained by integrating the response current density with time at different scan rates, where the value of Q* obtained at a scan rate of 0.005 $V \cdot s^{-1}$ reflects the total number of active sites (q_T) of the electrode [8]. Normal CV were obtained between 0 V (vs. SCE) and 2.5 V (vs. SCE) at a scan rate of 0.01 $V \cdot s^{-1}$, where the value of the response current density obtained at 2.5 V ($I_{2.5V}$) could reflect the electrocatalytic OER activity of the electrode [9]. Linear scanning voltammetry (LSV) were obtained between 0 V (vs. SCE) and 2.5 V (vs. SCE) with a scan rate of 0.001 $V \cdot s^{-1}$; the corresponding potential at 0.01 $A \cdot cm^{-1}$ was defined as the oxygen evolution potential (OEP, also reflecting OER activity) of the electrode [9]. Electrochemical impedance spectroscopy (EIS) was carried out with a range from 10^5 Hz to 0.1 Hz and an amplitude signal of 5 mV. The charge transfer resistance (R_{ct}) obtained at the equilibrium potential of 2 V (vs. SCE) could reflect the charge transfer in the OER process.

3.4. Wastewater Treatment

The azo dye ARG (Macklin, Shanghai, China) solution was selected as the synthetic wastewater (concentration 200 $mg \cdot L^{-1}$). Orthogonal tests were carried out using the orthogonal table of L_{27} (3^{13}) (the orthogonal test table is shown in Table S1) to obtain the levels of the significance factors affecting the ARG removal rate and COD removal rate. Therefore, six single factors including ME type (A), current density (B), AEs loading amount (C), AEs type (D), PDS concentration (E), and ultrasound power (F) were selected, each factor designed with three levels. The run time for each group of degradation experiments was 90 min, with samples taken at 0, 5, 10, 30, 60, and 90 min, respectively. Wastewater samples were tested (absorbance at 664 nm was taken to calculate ARG removal rate) using a UV-Vis spectrophotometer (TU-1810, Puxi, Beijing, China) [12]. The chemical oxygen demand (COD) of the solution was measured using a COD tester (ET 125 SC, Lovibond, Beijing, China) [29].

4. Conclusions

This study successfully integrated varying contents of Tml with the typical AEs Fe_3O_4/Sb-SnO_2 particles to develop novel AEs characterized by high catalytic activity and energy conversion properties. The MAE resulting from the combination with these novel AEs exhibits an increased number of active sites and a larger effective electrochemical active surface area. Notably, when loaded with SnO_2(4.5%T), the overall electrochemical performance of the electrode is maximally enhanced. Furthermore, it was observed that the AEs loading amount significantly influences ARG removal rate, and interactions between the AEs type and other factors are also noteworthy. The optimal ARG removal rate is achieved with 0.2 $g \cdot cm^{-2}$ SnO_2(4.5%T). Although current density and AEs type contribute minimally to the COD removal rate individually, their interaction markedly enhances this contribution rate, indicating that the AEs can only be activated when the waste energy and Tml synergistically work together. Both SnO_2(4.5%T) and SnO_2(16%T) effectively increase COD removal rate, with Tml's energy conversion function being pivotal in this enhancement process, significantly bolstering the mineralization capacity of MAE towards contaminants' degradation. In conclusion, this study demonstrates that an appropriate content of Tml within the AEs can efficiently harness the waste energy generated during electrochemical oxidation processes in water treatment applications while addressing issues related to insufficient and uneven polarization inherent in MAE. This research not only

offers a novel anode, but also paves the way for potential applications of energy conversion materials represented by Tml in electrochemical oxidation water treatment technology.

Supplementary Materials: The following supporting information can be downloaded at: https://www.mdpi.com/article/10.3390/catal15010002/s1, Figure S1: The SEM image of the Ti/Sb-SnO_2; Figure S2: Preparation process of SnO_2(0T), SnO_2(4.5%T) and SnO_2(16%T); Figure S3: SEM images and EDS elemental distributions of tourmaline and three AEs particles used in this study; Figure S4: XRD pattern of Tml; Figure S5: Difference in solution temperature during electrolysis at different current densities in this study; Figure S6: Narrow range cyclic voltammetry tests of 2D Ti/Sb-SnO_2 and 6 groups of MAE composed by Ti/Sb-SnO_2; Figure S7: Magnetic polarization curve of Tml; Figure S8: Ferroelectric properties of multiple Tml particle samples; Figure S9: The ARG removal rate by different MAE under different degradation conditions; Figure S10: Physical photographs of ARG decolorization at 90 min of degradation for 27 sets of orthogonal tests; Figures S11–S14: Results of orthogonal test analysis based on ARG removal rate after 5 min (Figure S11), 10 min (Figure S12), 60 min (Figure S13), and 90 min (Figure S14) of degradation; Figure S15: Possible degradation pathways for the ARG degradation; Figure S16: Fifteen cycles of ARG degradation experiments with the same degradation conditions performed on Sn/SnO_2(4.5%T)-0.2 g; Table S1: Levels of each factor; Table S2: L_{27} (3^{13}) table and L_{27} (3^{13}) table header; Table S3: The 27 groups of the experimental program table; Table S4: Analysis of variance table for ARG removal rate indexed by 30 min of degradation (non-significant factors were included in the pre-error); Table S5: Analysis of variance table for ARG removal rate indexed by 30 min of degradation (non-significant factors were included in the post error); Table S6: Contributions indexed by ARG removal rate at 30 min of degradation; Table S7: Factor main effects table indexed by ARG removal rate at 30 min of degradation; Table S8: B × D for ARG degradation for 30 min; Table S9: D × C for ARG degradation for 30 min. References [30–34] are cited in the supplementary materials.

Author Contributions: Conceptualization, B.Z. and D.S.; methodology, D.S.; validation, B.Z., D.S. and Y.W.; formal analysis, B.Z., D.S. and Y.W.; investigation, Y.W.; resources, D.S., H.X. and H.S.; data curation, B.Z. and Y.W.; writing—original draft preparation, B.Z. and Y.W.; writing—review and editing, B.Z., D.S. and Y.W.; visualization, B.Z. and Y.W.; supervision, D.S., H.X. and H.S.; project administration, D.S.; funding acquisition, D.S. All authors have read and agreed to the published version of the manuscript.

Funding: This research was funded by the National Natural Science Foundation of China (grant number: 21706153) and the Natural Science Basic Research Program of Shaanxi Province (grant number: 2022JM-065).

Data Availability Statement: The original data are included in the article and Supplementary Materials.

Acknowledgments: The authors acknowledge the financial support from the National Natural Science Foundation of China (21706153) and the Natural Science Basic Research Program of Shaanxi Province (2022JM-065).

Conflicts of Interest: The authors declare no conflicts of interest.

References

1. Miklos, D.B.; Remy, C.; Jekel, M.; Linden, K.G.; Drewes, J.E.; Hübner, U. Evaluation of advanced oxidation processes for water and wastewater treatment—A critical review. *Water Res.* **2018**, *139*, 118–131. [CrossRef] [PubMed]
2. Alkhadra, M.A.; Su, X.; Suss, M.E.; Tian, H.; Guyes, E.N.; Shocron, A.N.; Conforti, K.M.; de Souza, J.P.; Kim, N.; Tedesco, M.; et al. Electrochemical Methods for Water Purification, Ion Separations, and Energy Conversion. *Chem. Rev.* **2022**, *122*, 13547–13635. [CrossRef] [PubMed]
3. Dong, Y.; Yuan, H.; Ge, D.; Zhu, N. A novel conditioning approach for amelioration of sludge dewaterability using activated carbon strengthening electrochemical oxidation and realized mechanism. *Water Res.* **2022**, *220*, 118704. [CrossRef] [PubMed]
4. Yuan, Q.; Qu, S.; Li, R.; Huo, Z.-Y.; Gao, Y.; Luo, Y. Degradation of antibiotics by electrochemical advanced oxidation processes (EAOPs): Performance, mechanisms, and perspectives. *Sci. Total Environ.* **2023**, *856*, 159092. [CrossRef]

5. Xie, J.; Zhang, C.; Waite, T.D. Hydroxyl radicals in anodic oxidation systems: Generation, identification and quantification. *Water Res.* **2022**, *217*, 118425. [CrossRef]
6. Shao, D.; Zhang, X.-l.; Lyu, W.; Zhang, Y.; Tan, G.; Xu, H.; Yan, W. Magnetic Assembled Anode Combining PbO_2 and Sb-SnO_2 Organically as an Effective and Sustainable Electrocatalyst for Wastewater Treatment with Adjustable Attribution and Construction. *ACS Appl. Mater. Interfaces* **2018**, *10*, 44385–44395. [CrossRef] [PubMed]
7. Shao, D.; Lyu, W.; Cui, J.; Zhang, X.; Zhang, Y.; Tan, G.; Yan, W. Polyaniline nanoparticles magnetically coated Ti/Sb–SnO_2 electrode as a flexible and efficient electrocatalyst for boosted electrooxidation of biorefractory wastewater. *Chemosphere* **2020**, *241*, 125103. [CrossRef]
8. Zhang, Y.; Zhang, C.; Shao, D.; Xu, H.; Rao, Y.; Tan, G.; Yan, W. Magnetically assembled electrodes based on Pt, RuO_2-IrO_2-TiO_2 and Sb-SnO_2 for electrochemical oxidation of wastewater featured by fluctuant Cl-concentration. *J. Hazard. Mater.* **2022**, *421*, 126803. [CrossRef]
9. Shao, D.; Zhang, Y.; Lyu, W.; Zhang, X.-l.; Tan, G.; Xu, H.; Yan, W. A modular functionalized anode for efficient electrochemical oxidation of wastewater: Inseparable synergy between OER anode and its magnetic auxiliary electrodes. *J. Hazard. Mater.* **2020**, *390*, 122174. [CrossRef] [PubMed]
10. Shao, D.; Wang, Y.; Li, P.; Guo, R.; Zhang, Y.; Yang, C.; Yang, L.; Wei, Z.; Xu, H.; Yan, W.; et al. Integrating natural tourmaline with energy conversion ability to magnetically assembled electrode: Boosted electrochemical oxidation wastewater treatment performance. *J. Environ. Chem. Eng.* **2024**, *12*, 111664. [CrossRef]
11. Zhang, X.; Shao, D.; Lyu, W.; Xu, H.; Yang, L.; Zhang, Y.; Wang, Z.; Liu, P.; Yan, W.; Tan, G. Design of magnetically assembled electrode (MAE) with Ti/PbO_2 and heterogeneous auxiliary electrodes (AEs): The functionality of AEs for efficient electrochemical oxidation. *Chem. Eng. J.* **2020**, *395*, 125145. [CrossRef]
12. Zhang, F.; Shao, D.; Yang, C.; Xu, H.; Yang, J.; Feng, L.; Wang, S.; Li, Y.; Jia, X.; Song, H. New Magnetically Assembled Electrode Consisting of Magnetic Activated Carbon Particles and Ti/Sb-SnO_2 for a More Flexible and Cost-Effective Electrochemical Oxidation Wastewater Treatment. *Catalysts* **2023**, *13*, 7. [CrossRef]
13. Li, J.; Liu, X.; Zhao, G.; Liu, Z.; Cai, Y.; Wang, S.; Shen, C.; Hu, B.; Wang, X. Piezoelectric materials and techniques for environmental pollution remediation. *Sci. Total Environ.* **2023**, *869*, 161767. [CrossRef] [PubMed]
14. Zhou, L.; Yang, T.; Fang, Z.; Zhou, J.; Zheng, Y.; Guo, C.; Zhu, L.; Wang, E.; Hou, X.; Chou, K.-C.; et al. Boosting of water splitting using the chemical energy simultaneously harvested from light, kinetic energy and electrical energy using N doped 4H-SiC nanohole arrays. *Nano Energy* **2022**, *104*, 107876. [CrossRef]
15. Liu, W.; Wang, P.; Ao, Y.; Chen, J.; Gao, X.; Jia, B.; Ma, T. Directing Charge Transfer in a Chemical-Bonded $BaTiO_3$@ReS_2 Schottky Heterojunction for Piezoelectric Enhanced Photocatalysis. *Adv. Mater.* **2022**, *34*, e2202508. [CrossRef] [PubMed]
16. Ma, C.; Christianson, L.; Huang, X.; Christianson, R.; Cooke, R.A.; Bhattarai, R.; Li, S. Efficacy of heated tourmaline in reducing biomass clogging within woodchip bioreactors. *Sci. Total Environ.* **2021**, *755*, 142401. [CrossRef] [PubMed]
17. Liang, Y.; Tang, X.; Zhu, Q.; Han, J.; Wang, C. A review: Application of tourmaline in environmental fields. *Chemosphere* **2021**, *281*, 130780. [CrossRef]
18. Wu, Z.; Xu, T.; Wang, X.; Zhang, L.; Zhao, C.; Wu, W.; Zhu, G.; Jia, Y. Natural tourmaline for pyroelectric dye decomposition under 25–60 °C room-temperature cold-hot fluctuation. *Sep. Purif. Technol.* **2023**, *327*, 124971. [CrossRef]
19. Wang, W.; Liu, X.; Li, K.; Li, T. Dechlorinating performance of *Dehalococcoides* spp. mixed culture enhanced by tourmaline. *Chemosphere* **2018**, *194*, 9–19. [CrossRef]
20. Zong, L.; Yu, Y.; Wang, J.; Liu, P.; Feng, W.; Dai, X.; Chen, L.; Gunawan, C.; Jimmy Yun, S.L.; Amal, R.; et al. Oxygen-vacancy-rich molybdenum carbide MXene nanonetworks for ultrasound-triggered and capturing-enhanced sonocatalytic bacteria eradication. *Biomaterials* **2023**, *296*, 122074. [CrossRef]
21. An, C.; Wang, T.; Wang, S.; Chen, X.; Han, X.; Wu, S.; Deng, Q.; Zhao, L.; Hu, N. Ultrasonic-assisted preparation of two-dimensional materials for electrocatalysts. *Ultrason. Sonochem.* **2023**, *98*, 106503. [CrossRef] [PubMed]
22. Ismael, M. Photo-Fenton reaction enhanced visible-light activity of p- Photo-Fenton reaction enhanced visible-light activity of p-$CuFe_2O_4$/n-g-C_3N_4 heterojunction composites synthesized by a simple ultrasonic-assisted route for organic pollutants degradation. *Mater. Res. Bull.* **2022**, *151*, 111803. [CrossRef]
23. Yang, X.L.; Yang, X.; Peng, Y.; Li, Z.-F.; Yu, J.; Zhang, Y. Regulating the Built-In Electric Field of BiOBr by a Piezoelectric Mineral Tourmaline and the Enhanced Photocatalytic Property. *Ind. Eng. Chem. Res.* **2022**, *61*, 1704–1714. [CrossRef]
24. Sun, S.; Li, J.; Ding, H.; Zhang, B.; Huang, H.; Xu, Z.; Tu, Y.; Chen, D.; Duan, X. Engineered tourmaline/g-C_3N_4 composites for photocatalytic Fenton-like oxidation: Synergy of spontaneous interface polarization and surface iron circulations induced by minerals. *Chem. Eng. J.* **2023**, *460*, 141718. [CrossRef]
25. Voiry, D.; Chhowalla, M.; Gogotsi, Y.; Kotov, N.A.; Li, Y.; Penner, R.M.; Schaak, R.E.; Weiss, P.S. Best Practices for Reporting Electrocatalytic Performance of Nanomaterials. *ACS Nano* **2018**, *12*, 9635–9638. [CrossRef] [PubMed]
26. Liu, Z.; Ren, X.; Duan, X.; Sarmah, A.K.; Zhao, X. Remediation of environmentally persistent organic pollutants (POPs) by persulfates oxidation system (PS): A review. *Sci. Total Environ.* **2022**, *863*, 160818. [CrossRef] [PubMed]

27. Moyé, L. Statistical Methods for Cardiovascular Researchers. *Circul. Res.* **2016**, *118*, 439–453. [CrossRef]
28. Song, B.; Liang, H.; Sun, R.; Peng, P.; Jiang, Y.; She, D. Hydrogel synthesis based on lignin/sodium alginate and application in agriculture. *Int. J. Biol. Macromol.* **2020**, *144*, 219–230. [CrossRef] [PubMed]
29. Park, J.W.; Kim, S.Y.; Noh, J.H.; Bae, Y.H.; Lee, J.W.; Maeng, S.K. A shift from chemical oxygen demand to total organic carbon for stringent industrial wastewater regulations: Utilization of organic matter characteristics. *J. Environ. Manag.* **2022**, *305*, 114412. [CrossRef] [PubMed]
30. Shao, D.; Yan, W.; Li, X.; Xu, H. Fe_3O_4/Sb–SnO_2 granules loaded on Ti/Sb–SnO_2 electrode shell by magnetic force: Good recyclability and high electro-oxidation performance. *ACS Sustain. Chem. Eng.* **2015**, *3*, 1777–1785. [CrossRef]
31. Shao, D.; Zhao, W.; Ji, S.; Yang, C.; Zhang, J.; Guo, R.; Zhang, B.; Lyu, W.; Feng, J.; Xu, H.; et al. Joule heat assisting electrochemical degradation of polyethylene microplastics melted on anode. *Appl. Catal. B Environ. Energy* **2024**, *357*, 124281. [CrossRef]
32. Thomas, S.; Sreekanth, R.; Sijumon, V.A.; Aravind, U.K.; Aravindakumar, C.T. Oxidative degradation of Acid Red 1 in aqueous medium. *Chem. Eng. J.* **2014**, *244*, 473–482. [CrossRef]
33. Muni, R.N.; Singh, J.; Kumar, V.; Sharma, S.; Sudhakara, P.; Aggarwal, V.; Rajkumar, S. Multiobjective optimization of EDM parameters for rice husk Ash/Cu/Mg-reinforced hybrid Al-0.7Fe-0.6Si-0.375Cr-0.25Zn metal matrix nanocomposites for engineering applications: Fabrication and morphological analysis. *J. Nanomater.* **2022**, *2022*, 2188705. [CrossRef]
34. Florenza, X.; Solano, A.M.S.; Centellas, F.; Martínez-Huitle, C.A.; Brillas, E.; Garcia-Segura, S. Degradation of the azo dye Acid Red 1 by anodic oxidation and indirect electrochemical processes based on Fenton's reaction chemistry. Relationship between decolorization, mineralization and products. *Electrochim. Acta* **2014**, *142*, 276–288. [CrossRef]

Disclaimer/Publisher's Note: The statements, opinions and data contained in all publications are solely those of the individual author(s) and contributor(s) and not of MDPI and/or the editor(s). MDPI and/or the editor(s) disclaim responsibility for any injury to people or property resulting from any ideas, methods, instructions or products referred to in the content.